(Received 27 April 2026, Accepted 1 June 2026, Scheduled 18 June 2026)

Design and Analysis of a Multi-Tooth Flux-Switching PM Machine with HTS Bulks and Flux Reversal Effect

Zeyu Min, Zezhou Jin, Lingzi Min, and Libing Jing*

College of Electrical Engineering and New Energy, Hubei Provincial Engineering Technology Research Center for Microgrid China Three Gorges University, Yichang 443002, China

ABSTRACT: This paper presents a novel multi-tooth flux-switching permanent magnet (MT-FSPM) machine that incorporates HTS bulks and radially magnetized PMs within the stator teeth. The alternating arrangement of PMs produces a synergistic effect between the flux-reversal mechanism and flux-switching mechanism. Additionally, the magnetic flux shielding effect of HTS materials effectively reduces flux leakage from the stator teeth, thereby enhancing the output torque. Subsequently, parameterized finite element models of the conventional and proposed models were established, and the key design parameters were systematically stratified based on sensitivity analysis. The optimal values for the high-sensitivity parameters were then obtained using the response surface method (RSM) and multi-objective genetic algorithm (MOGA). Finally, compared with the conventional model, the results demonstrate that the proposed model achieves a significant enhancement in torque performance, with the output torque increased by 49.69% and torque ripple reduced by 16.90%. Furthermore, the proposed model exhibits superior overload capability and improved power factor.

1. INTRODUCTION

Superconducting materials, characterized by zero electrical resistance and flux capture capabilities, enable electric machines to operate with minimal energy loss, thereby significantly improving efficiency [1, 2]. Additionally, with the development of High-Temperature Superconducting (HTS) materials and low-temperature technology, superconducting machines have become a research hotspot in the field of drive machines [3].

Stator permanent magnet (PM) machines, with both the PMs and windings placed on the stator, facilitate direct cooling and better temperature rise control, making such machines promising candidates for superconducting machines. In [4], a flux-switching PM (FSPM) machine employing a single ring-shaped HTS excitation coil is proposed, achieving physical isolation between the armature winding and the excitation coil, thereby improving cooling and torque performance. In addition, an HTS coil is applied to the dual-rotor FSPM machine in [5], which not only effectively reduces the weight and losses of the machine but also enhances power density and efficiency. From the perspective of reducing flux leakage, a spoke-type PM combined with an HTS disc-type axial FSPM machine is discussed in [6], in which the HTS disc effectively prevents magnetic flux from entering or exiting, thereby increasing torque density. Therefore, the introduction of HTS materials can effectively improve electromagnetic performance and space utilization of electrical machines.

In direct-drive applications, to meet the demand for high-torque transmission within a compact volume, dual-PM machines integrate dual-PM excitation, demonstrating a higher torque density than traditional single-PM machines [7, 8]. By combining the stator and rotor PMs, a modular linear doubly salient machine with dual-PM excitation is proposed in [9]. The dual-PM flux improves the torque output by enhancing the air-gap flux density. Furthermore, based on the air-gap magnetic field modulation mechanism, a synergistic modulation effect of stator and rotor permeance is designed to improve the air-gap magnetic field generated by double-sided PMs, thereby enhancing the torque performance of the machine [10]. However, placing PMs on the rotor introduces challenges, such as high centrifugal force, extra reinforcement requirements, and a larger effective air gap. In addition, the rotor is difficult to cool during rotation, and the resulting temperature rise can cause irreversible demagnetization, affecting the reliability of the machine. Therefore, to overcome these drawbacks, the arrangement of dual PMs on the stator side is a better choice [11]. In [12], two differently magnetized PMs in the stator teeth of multi-tooth FSPM (MT-FSPM) machines are proposed. This dual-PM effect effectively increased the output torque. However, the improvement in torque performance is inevitably accompanied by an increase in the amount of PM material.

FSPM and Flux Reversal PM (FRPM) machines, as representatives of stator PM machines, are characterized by bipolar magnetic flux linkage and high torque density. Compared to the traditional FRPM machine, the alternate-pole structure requires only half amount of PM material. However, owing to the smaller effective air gap and reduced magnetic leakage in the alternate-pole structure, the no-load magnetic flux linkage is actually greater than that of traditional structures [13]. Consequently, many researchers have proposed various novel topological structures [14, 15].

* Corresponding author: Libing Jing (jinglibing163@163.com).

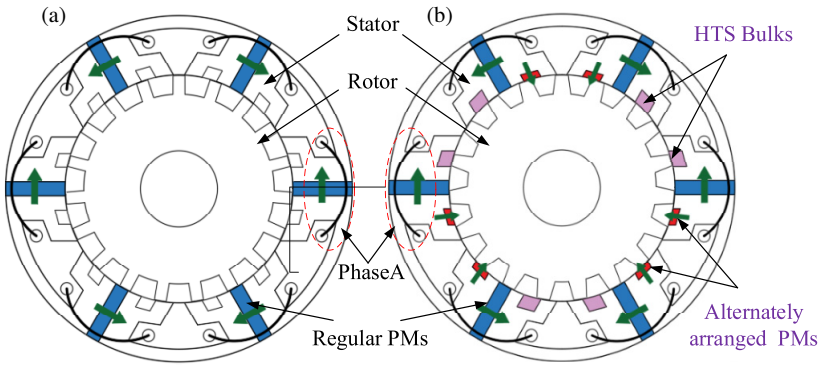

FIGURE 1. Topology of MT-FSPM machine: (a) Conventional and (b) the proposed.

Based on the alternate arrangement of PMs and HTS bulks in the stator teeth, this paper proposes a novel MT-FSPM machine that incorporates both flux switching effect and flux-reversal effect. The key parameters of the machine are optimized in Section 3. A comparative analysis of the electromagnetic performance between the proposed and conventional machines is conducted in Section 4. Finally, this paper concludes with a summary of the findings in Section 5.

2. TOPOLOGY AND OPERATION PRINCIPLE

Figure 1 presents a comparison between the conventional and proposed topologies. The proposed design incorporates HTS bulks and PMs within the stator teeth, arranged alternately in the sequence of HTS-HTS-PM-PM. The green arrows indicate the magnetization direction of the PMs, showing that all the arranged PMs are magnetized downward. The synergy between the HTS bulks and radially magnetized PMs effectively reduces the flux leakage within the stator teeth, thereby enhancing the working harmonics in the air gap and improving torque performance. Based on the finite element analysis, Fig. 2 shows the magnetic field distribution at the same rotor angle under open circuit conditions. Taking the A-phase winding as an example, the results show that the no-load flux linkage reaches the maximum value at the same time under the flux switching and Flux Reversal Effect.

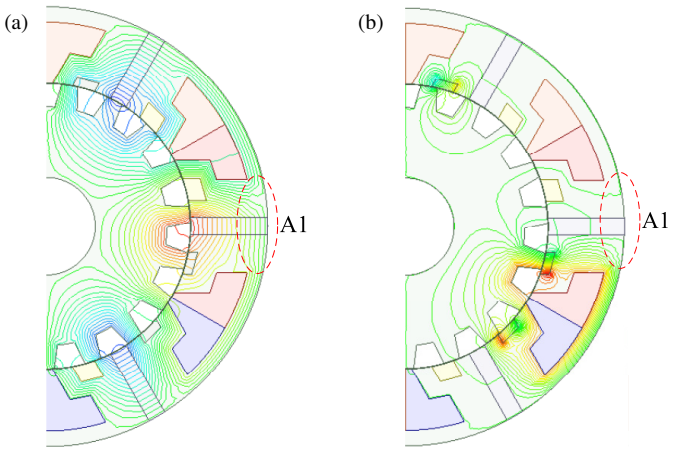

FIGURE 2. Field distributions. (a) Maximum flux-linkage of flux switching effect with coil A1 and (b) Maximum flux-linkage of Flux Reversal Effect with coil A1.

Based on the permeance-magnetomotive force (MMF) model, the PM MMF of the FSPM and FRPM can be expressed as,

$$\begin{cases} F_{\text{SPM}} = \frac{4F_S}{\pi} \sum\limits_{n=1,3,5\ldots}^{\infty} F_{\text{SPM}n} \sin(nP_S\theta) \\ F_{\text{SPM}n} = \frac{\cos nP_S\theta_1}{n} \end{cases}$$

$$\begin{cases} F_{\text{RPM}} = \frac{4F_R}{\pi} \sum\limits_{n=1,3,5\ldots}^{\infty} F_{\text{RPM}n} \sin(nP_R\theta) \\ F_{\text{RPM}n} = \frac{\cos nP_R\theta_3 - \cos nP_R\theta_2}{n} \end{cases} \quad (1)$$

where F_S and P_S are the amplitude and pole pair number of the tangentially magnetized PMs, respectively; F_R and P_R are the amplitude and pole pair number of the radially magnetized PMs, respectively; θ_1 is half of the pole arc coefficient of the tangentially magnetized PMs; θ_2 is the angle between the radially magnetized PMs and stator centerline; and θ_3 is the pole arc coefficient of the radially magnetized PMs.

For the doubly saliency structure, the air-gap permeance function can be given as [16]

$$P_r(\theta,t) = P_{r0} + \sum_{k=1,2,3\ldots} P_{rk} \cos\left[kZ_r\left(\theta - \omega_r t - \theta_0\right)\right] \quad (2)$$

where P_{r0} and P_{rk} are the DC component and the kth harmonic component of the rotor permeance, respectively; ω_r is the mechanical rotational angular velocity; θ_0 is the angular position of the rotor measured in the stationary coordinate system; Z_r is the number of rotor pole pieces. Then, through rotor permeance modulation, the no-load magnetic flux density in the air gap $B_{\text{PM}}(\theta,t)$ can be obtained as follows

$$B_{\text{PM}}(\theta,t) = (F_{\text{SPM}} + F_{\text{RPM}})P_r(\theta,t) = \frac{2P_{r0}}{\pi}$$

$$\sum_{n=1,3,5\ldots}^{\infty} (F_s F_{\text{SPM}n} + F_{\text{RPM}n}F_{\text{PM}n}) \sin(nP\theta)$$

$$\frac{2F_s}{\pi} \sum_{n=1,3,5\ldots}^{\infty} \sum_{k=1}^{\infty} F_{\text{SPM}n}P_{rk} \sin[(nP \pm kZ_r\theta$$

$$-(kZ_r\omega_r t \mp kZ_r\theta_0)]$$

$$-\frac{2F_R}{\pi}\sum_{n=1,3,5\ldots}^{\infty}\sum_{k=1}^{\infty}F_{\mathrm{RPM}n}P_{rk}\sin[(nP \pm kZ_r\theta$$

$$-(kZ_r\omega_r t \mp kZ_r\theta_0)] \quad (3)$$

Combining with the winding function $N(\theta)$, the permanent magnet flux linked can be calculated as,

$$\begin{aligned}\psi(t) &= k_w r_g l_s \int_0^{2\pi} B_{\mathrm{PM}}(\theta,t)N(\theta)d\theta \\ &= k_w r_g l_s \int_0^{2\pi} \sum_{\substack{n=1,3,5\ldots\\ j=1,2,3\ldots}}^{\infty} F_n P_{r1} N_{wj} \sin\left[(nP_S \pm Z_r)\,\theta\right. \\ &\quad \left. -Z_r\omega_r t\right]\cos\left(jP_w\theta\right)d\theta \\ &\quad + k_w r_g l_s \int_0^{2\pi} \sum_{\substack{n=1,3,5\ldots\\ j=1,2,3\ldots}}^{\infty} F_n P_{r1} N_{wj} \sin\left[(nP_R \pm Z_r)\,\theta\right. \\ &\quad \left. -Z_r\omega_r t\right]\cos\left(jP_w\theta\right)d\theta \end{aligned} \quad (4)$$

where k_w denotes the winding coefficient, and l_s and r_g represent the stack length and air-gap radius, respectively.

According to formula (4), the flux linkage contributions under the two effects can be obtained respectively, as shown in Fig. 3. The no-load flux linkage distribution under flux switching and flux reversal effects is highly consistent. This indicates that the magnetic fields generated by the radially magnetized PM arranged in the stator teeth and the original tangentially magnetized PM can be effectively coordinated, enhancing the magnetic flux through the winding turn chain.

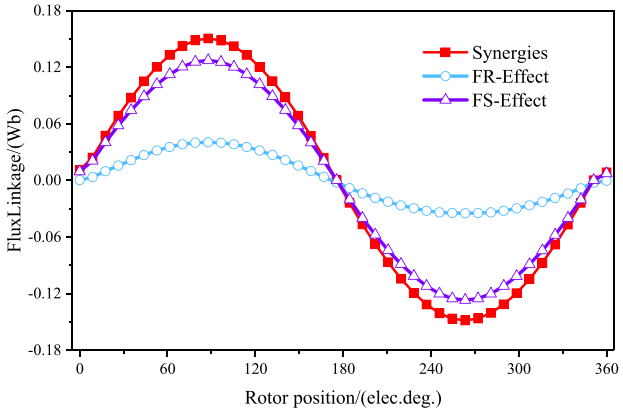

FIGURE 3. The Phase A flux linkage of flux switching and Flux Reversal Effect.

Figure 4 illustrates the structure of the HTS bulk. It primarily consists of YBCO material, a carbon fiber frame, coolant, and a vacuum chamber. YBCO reaches a superconducting state at 77 K, which is higher than the boiling point of liquid nitrogen and can be cooled by introducing circulating liquid nitrogen through a liquid pipeline, whereas the vacuum chamber provides thermal insulation. By ensuring that the HTS material

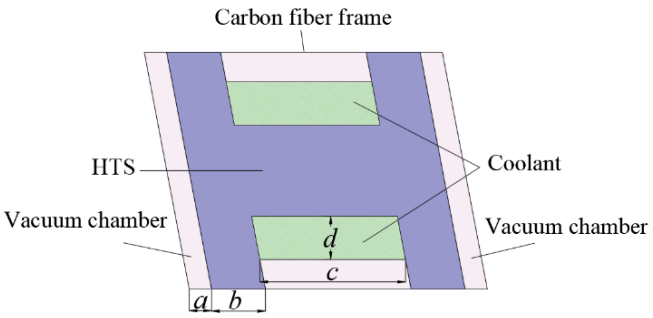

FIGURE 4. Structure of HTS bulk.

thickness is significantly greater than the London penetration depth, the YBCO enters a superconducting state when operated below its critical temperature. This state effectively prevents external magnetic fields from penetrating the internal structure and reduces magnetic flux leakage between the stator teeth. The basic parameters of the MT-FSPM machine, along with the dimensions of the superconducting material, are listed in Table 1. Except for the HTS material, all other basic parameters of the conventional machine are identical to those of the proposed machine. Moreover, although radially magnetized PMs are introduced in the proposed machine, the total PM volume is constrained to be almost the same as that of the conventional machine during the optimization process.

TABLE 1. Basic parameters of MT-FSPM machine.

Quantity	Conventional machine	Proposed machine
Number of phases	3	
Number of stator poles	6	
Number of rotor poles	19	
Number of coils	50	
Rated current/I_{rms} (A)	35	
Stator outer radius/mm	144	
Rotor inner radius/mm	32	
Stack length/mm	85	
Air gap length/mm	0.5	
Total PM volume/mm^3	360.1	362.7
Number of HTS bulks	/	6
HTS material	/	YBCO
Vacuum chamber thickness/a (mm)	/	1
HTS thickness/b (mm)	/	2.5
Coolant length/c (mm)	/	7
Coolant width/d (mm)	/	3

3. KEY PARAMETERS OPTIMIZATION

In the design process of the MT-FPSM machine, the performance machine is influenced by multiple design parameters, and there is a complex interdependence between the parameters. Therefore, determining the optimal combination of parameters to meet the crucial performance criteria is a signifi-

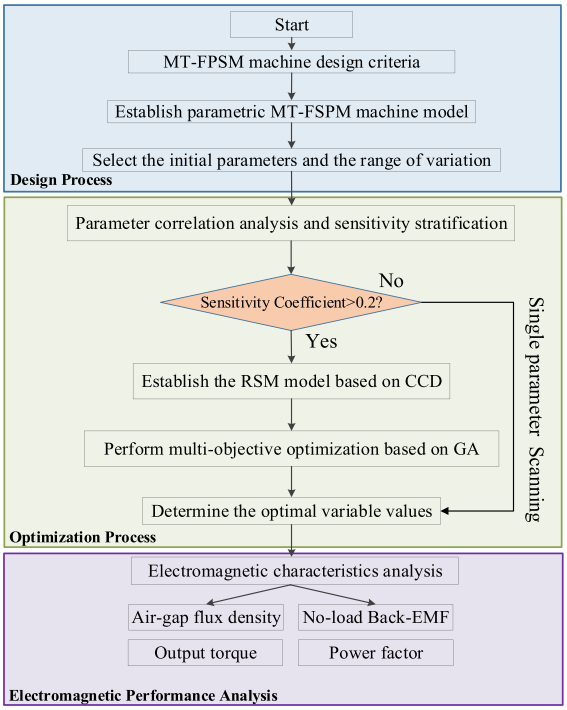

FIGURE 5. Design flow chart.

cant challenge in the design process. Based on multi-objective optimization, this paper presents the overall design flow for the MT-FPSM machine, as illustrated in Fig. 5. The design process is divided into three parts. In the optimization process, a sensitivity-coefficient-based stratification approach is adopted: low-sensitivity variables are analyzed via single-parameter scanning, while high-sensitivity variables are optimized using a genetic algorithm based on the response surface to obtain optimal values. The key parameters include the geometric dimensions of the PM, rotor, and stator, such as the rotor tooth radian, PM width, and stator tooth width, as illustrated in Fig. 6.

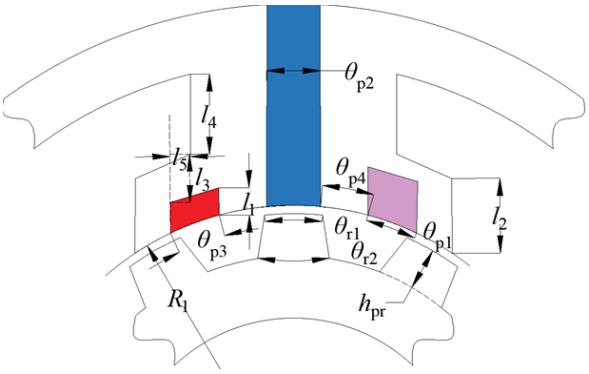

FIGURE 6. Key parameters of proposed machine.

3.1. Comprehensive Sensitivity Analysis

In the optimization design process, the large number of design variables, involving exerting varying degrees of influence on the optimization objective, motivates the adoption of sensitivity analysis to reduce computational cost. This method quantifies the impact of each design variable on the optimization objectives, identifies key variables, and mitigates effects of inter-variable coupling. The comprehensive sensitivity coefficient can be expressed as,

$$S_j(x_i) = V\left(E\left(y_j/x_i\right)\right)/V\left(y_j\right) \tag{5}$$

where x_i denotes the ith design variable, y_j the jth optimization objective, $E(y_j/x_i)$ the expected value of y_j when x_i is a constant, $V(E(y_j/x_i))$ the variance of $E(y_j/x_i)$, $V(y_j)$ the variance of y_j, and $S_j(x_i)$ the sensitivity of the ith design variable to the jth optimization objective. In this study, the torque ripple and average torque are selected as the two optimization objectives.

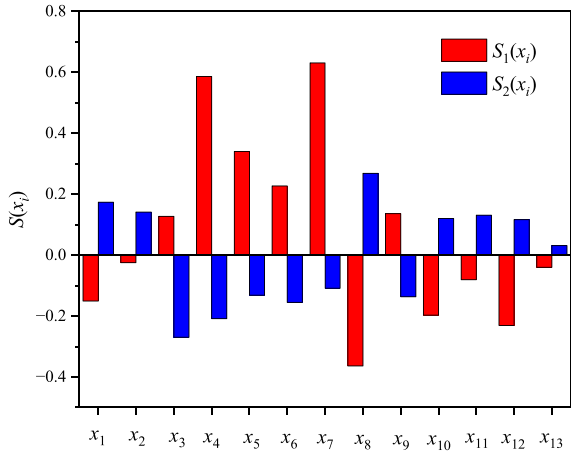

FIGURE 7. Design variable sensitivity analysis results.

Figure 7 reveals the sensitivity of each design variable to the different optimization objectives, and the sensitivity coefficients of x_4, x_5, x_6, and x_8 exhibit relatively larger sensitivity coefficients, which identify them as high-sensitivity variables. Generally, a higher sensitivity coefficient reflects a stronger functional relationship between the design variable and optimization objective. A positive sensitivity indicates that the optimization objective increases with the design variable, while a negative sensitivity suggests an inverse correlation. To simultaneously address multiple optimization objectives, a weighting coefficient is introduced to stratify and effectively assess the influence of each design variable, as expressed by the following formula,

$$\begin{cases} S_{\text{com}}\left(x_i\right) = \lambda_1 \left|S_1\left(x_i\right)\right| + \lambda_2 \left|S_2\left(x_i\right)\right| \\ \lambda_1 + \lambda_2 = 1 \end{cases} \tag{6}$$

where $S_{\text{com}}(x_i)$ denotes the comprehensive sensitivity of the ith variable; $S_1(x_i)$ represents the sensitivity value of the ith variable to the average torque; $S_2(x_i)$ denotes the sensitivity value of the ith variable to the torque ripple; λ_1 and λ_2 are the weight coefficients of the multi-objective optimization function. Considering that the proposed topology in this paper is aimed at reducing flux leakage and enhancing the flux linkage coupling effect to improve the average torque, the average torque $S_1(x_i)$ is prioritized in the optimization objectives. Therefore, the weight coefficient λ_1 is set to 0.6, while the $S_2(x_i)$ is assigned a lower priority with $\lambda_2 = 0.4$. Based on these weight coefficients, the

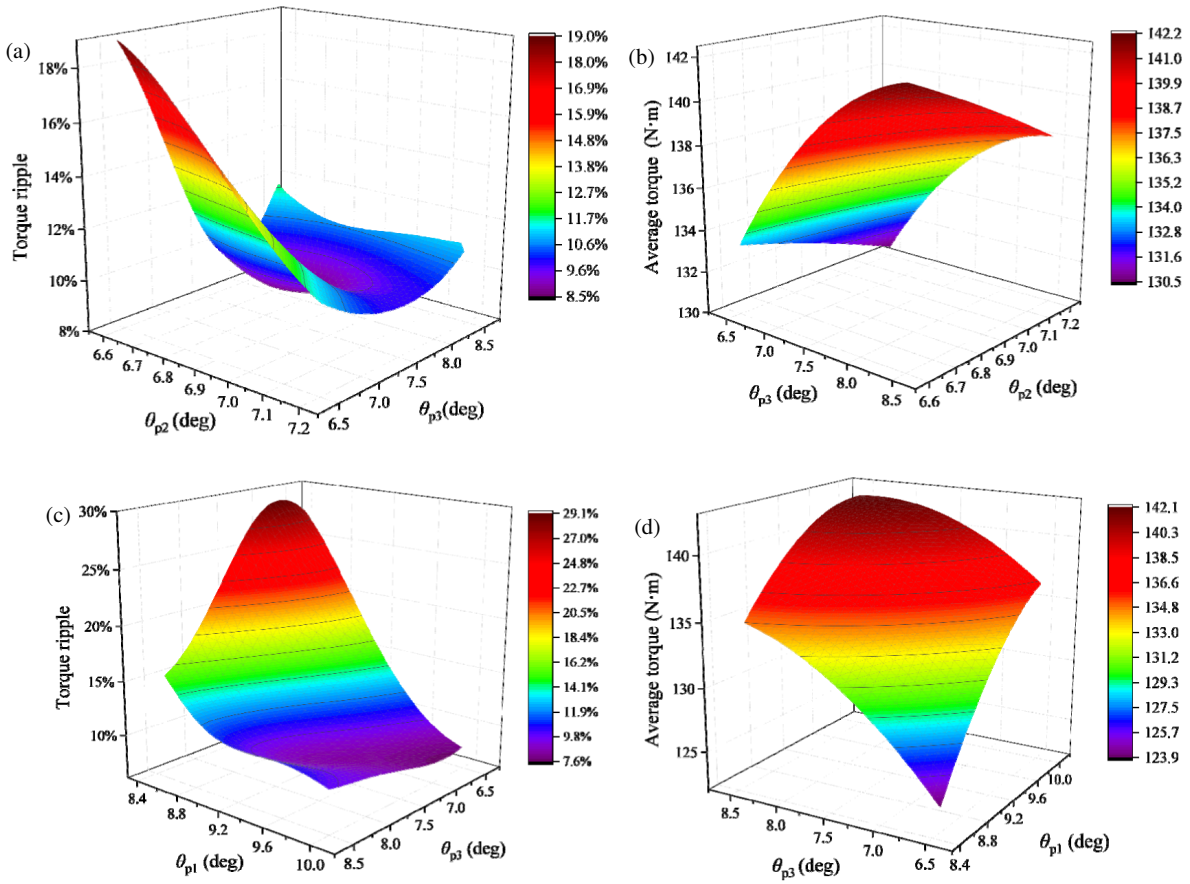

FIGURE 8. Responses surface of optimization objectives.

calculated comprehensive sensitivity coefficients of the design variables are presented in Table 2.

3.2. Response Surface Model

To clearly reveal the relationship between the response objectives and design variables, this study employs the response surface method for analysis, aiming to efficiently evaluate the design impacts with fewer experiments. Among the various response surface methods, Central Composite Design (CCD) and Box-Behnken Design (BBD) are the most widely employed. Compared with BBD, CCD introduces axial points, which allow it to cover a wider range of factor levels and make it more suitable for fitting higher-order response surfaces and analyzing boundary nonlinearities. Moreover, CCD possesses rotatability, which ensures uniform prediction variance in all directions, and the replication of center points facilitates accurate estimation of pure error and lack-of-fit. Based on CCD, the constructed response surface model can be expressed as follows

$$y = \beta_0 + \sum_{i=1}^{k} \beta_i x_i + \sum_{i=1}^{k} \beta_{ii} x_i^2 + \sum_{i<j} \beta_{ij} x_i x_j + \delta \quad (7)$$

where y is the predicted value of S_1 or S_2; β_0 is the constant term, β_i and β_{ii} are the coefficients of the linear and quadratic terms of the design variables; β_{ij} are the coefficients of the interaction terms; δ is the statistical error.

TABLE 2. Comprehensive sensitivity index.

Design Variables		$\lvert S_1(x_i)\rvert$ $\lambda_1 = 0.6$	$\lvert S_2(x_i)\rvert$ $\lambda_2 = 0.4$	$S_{\text{com}}(x_i)$
x_1	R_1	0.151	0.173	0.160
x_2	θ_{r1}	0.025	0.141	0.071
x_3	θ_{r2}	0.127	0.270	0.184
x_4	θ_{p1}	0.586	0.209	0.435
x_5	θ_{p2}	0.340	0.132	0.257
x_6	θ_{p3}	0.2267	0.155	0.222
x_7	θ_{p4}	0.063	0.109	0.081
x_8	l_1	0.364	0.268	0.326
x_9	l_2	0.136	0.137	0.136
x_{10}	l_3	0.197	0.120	0.166
x_{11}	l_4	0.081	0.131	0.101
x_{12}	l_5	0.231	0.116	0.185
x_{13}	h_{pr}	0.040	0.031	0.036

Taking the design variables θ_{p1}, θ_{p2}, and θ_{p3} as examples, Fig. 8 shows the response surfaces for the two optimization objectives. It can be observed that with the increase of θ_{p1}, the torque ripple generally exhibits a trend of first decreasing and then slightly fluctuating, while the average torque increases gradually. As θ_{p2} increases, the torque ripple first decreases significantly and then increases slowly, and the average torque

shows an overall gradual increasing trend. With the increase of θ_{p3}, the torque ripple decreases rapidly first and then fluctuates slightly, while the average torque increases gradually.

3.3. MOGA Optimization

Through the multi-objective optimization approach, the complex coupling between parameters is effectively addressed. The Multi-Objective Genetic Algorithm (MOGA) can independently handle multiple optimization objectives without the need to combine them into a single objective function [17]. By exploring a wide solution space, it generates a set of Pareto optimal solutions, allowing for a balanced trade-off between conflicting objectives. The multi-objective optimization function can be expressed as follows,

$$\begin{cases} \text{Obj}: \begin{cases} \text{Max}(T_{\text{avg}}(x)) \\ \text{Min}(T_{\text{rip}}(x)) \end{cases} \\ \text{s.t.}: \ x_{\min} < x_i < x_{\max} \ (i = 1, 2, 3) \end{cases} \tag{8}$$

where x_i is the design parameter, and the maximum $T_{\text{avg}}(x)$ and minimum $T_{\text{rip}}(x)$ are the optimization objectives.

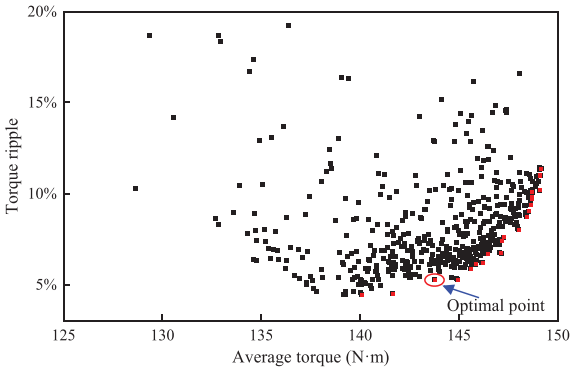

FIGURE 9. Optimization result based on MOGA.

As shown in Fig. 9, the torque ripple and torque are optimized based on the MOGA. The black points represent all design points, and the red points denote the Pareto front points. The selected optimal point is indicated by a blue arrow, showing that the torque ripple is approximately 5% at a torque of approximately 145 N·m. The design parameter values corresponding to this optimal point are listed in Table 3.

TABLE 3. Design parameter optimization value.

Parameter	Optimal
x_4/θ_{p1} (deg)	9.67
x_5/θ_{p2} (deg)	6.88
x_6/θ_{p3} (deg)	8.25
x_8/l_1 (mm)	5.11

4. ELECTROMAGNETIC PERFORMANCE ANALYSIS

In this section, the crucial electromagnetic performance of the proposed machine is analyzed and compared with that of a conventional machine based on the two-dimensional (2D) finite element analysis (FEA).

4.1. No-Load Magnetic Field

Figure 10 illustrates the flux distribution in the proposed machine. It can be observed that the arrangement of HTS bulks allows magnetic flux lines to be more effectively concentrated and smoothly guided when they pass through the stator teeth and reduces the magnetic flux leakage from the stator teeth. This effect directly enhances the flux linkage in the windings and increases the contribution of the magnetomotive force to the torque, thereby achieving a higher torque output.

Figure 11(a) shows a comparison of the no-load air-gap flux density waveforms. According to the formula (3), with the pole pair number of PMs being 3, the harmonic components corresponding to the 3rd, 9th, 21st, and 27th pole pairs are stationary. In contrast, harmonics, such as the 4th and 16th pole pairs, are rotating harmonic components generated by rotor modulation. Different combinations of modulation coefficients n and j can modulate the magnetic field harmonics of various pole-pair numbers. Consequently, the spectrum of the PM magnetic field harmonics in the MT-FSPM machine, as shown in Fig. 11(b), is abundant. Among the various working harmonics, the 15th and 21st harmonics exhibit consistent harmonic characteristics and initial phase relationships between the no-load field and the armature field. With relatively high amplitudes, the 15th and 21st harmonics are defined as the primary working harmonics. These harmonics are significantly enhanced in the proposed machine and make the dominant positive contribution to torque. Although the amplitudes of the 3rd, 16th, and 22nd harmonics are slightly lower than those of the conventional machine, the torque contribution of the 3rd harmonic is negligible after coupling with the armature reaction field. Figure 12 illustrates the waveform and spectral analysis of the no-load back-electromotive force (EMF). The proposed machine achieves a back-EMF (electromotive force) amplitude of 456.82 V, which represents an increase of 9.04% compared with 418.95 V of the conventional machine. Furthermore, the total harmonic distortion (THD) can be expressed as follows,

$$\text{THD} = \frac{\sqrt{\sum_{i=2}^{\infty} k_i^2}}{k_1} \times 100\% \tag{9}$$

where k_i is the ith harmonic amplitude, k_1 the fundamental amplitude, and i the harmonic order. The fundamental amplitude of the proposed machine is 442.51 V, with a THD of 2.63%, whereas the conventional machine has a fundamental amplitude of 424.49 V and a THD of 2.31%. Although the proposed machine exhibits a slightly higher THD, it still maintains the machine's high sinusoidal characteristic.

4.2. Output Torque and Overload Capability

Figure 13 presents a comparison of the output torque. The conventional machine exhibits an average output torque of 95.66 N·m with a torque ripple of 6.33%. In contrast, the pro-

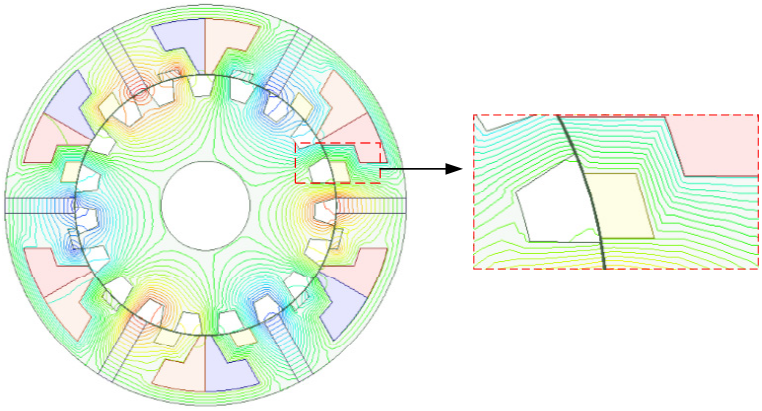

FIGURE 10. Flux distributions.

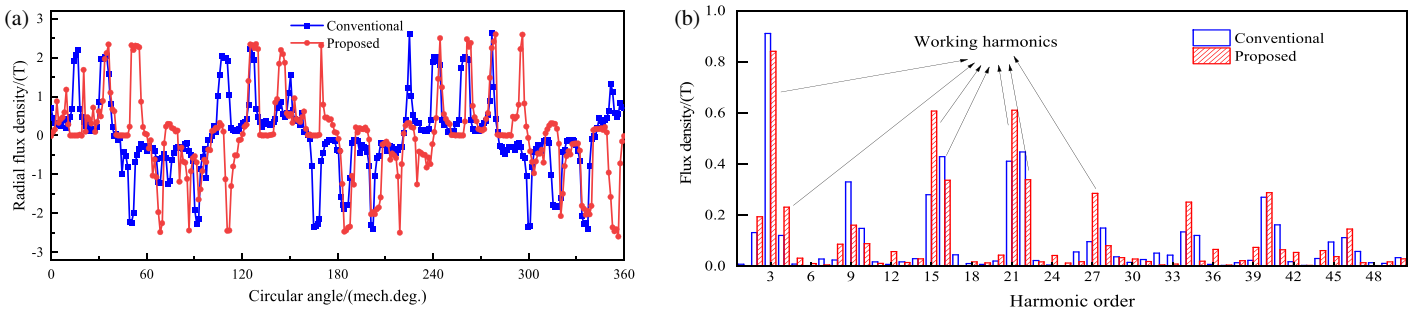

FIGURE 11. No-load radial air gap magnetic density: (a) Waveform, (b) spectral analysis.

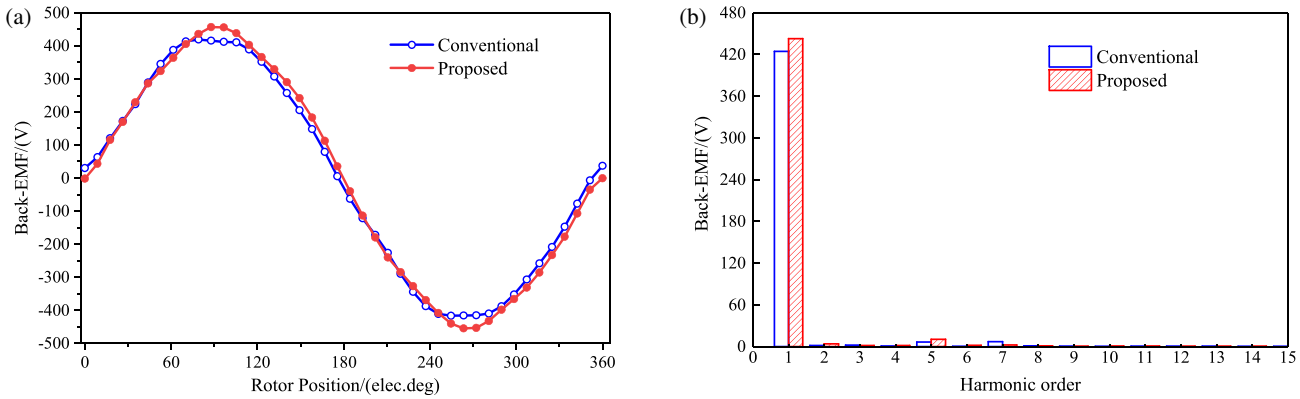

FIGURE 12. No-load back-EMF: (a) Waveform, (b) spectral analysis.

posed machine achieves an output torque of 143.19 N·m, representing a 49.69% increase. Additionally, the torque ripple of the proposed machine is reduced to 5.26%, a decrease of 16.90%. These results indicate that the proposed machine not only significantly enhances the output torque but also demonstrates superior torque stability. Fig. 13(b) illustrates the torque contributions of the individual harmonic components. Notably, the 15th and 21st harmonic components exhibit substantially enhanced torque contributions, a trend that aligns consistently with the harmonic characteristics observed in the no-load air-gap magnetic field. These results indicate that the proposed machine design effectively strengthens the rotor modulation effect, thereby amplifying the rotating working harmonic fields responsible for torque generation.

Figure 14 further compares the overload performance of the two machines. As the current increases, the average torque of both machines rises and gradually approaches saturation at high current levels. Notably, under various load conditions, the proposed machine consistently generates higher torque than the conventional machine.

4.3. Power Factor

The power factor is a crucial metric for assessing the efficiency with which a motor converts input electrical energy into useful output power. The expression is as follows

$$\mathrm{PF} = \cos\theta = 1/\sqrt{1 + (\omega_e L_s I_s / E_{\mathrm{ph}})^2} \tag{10}$$

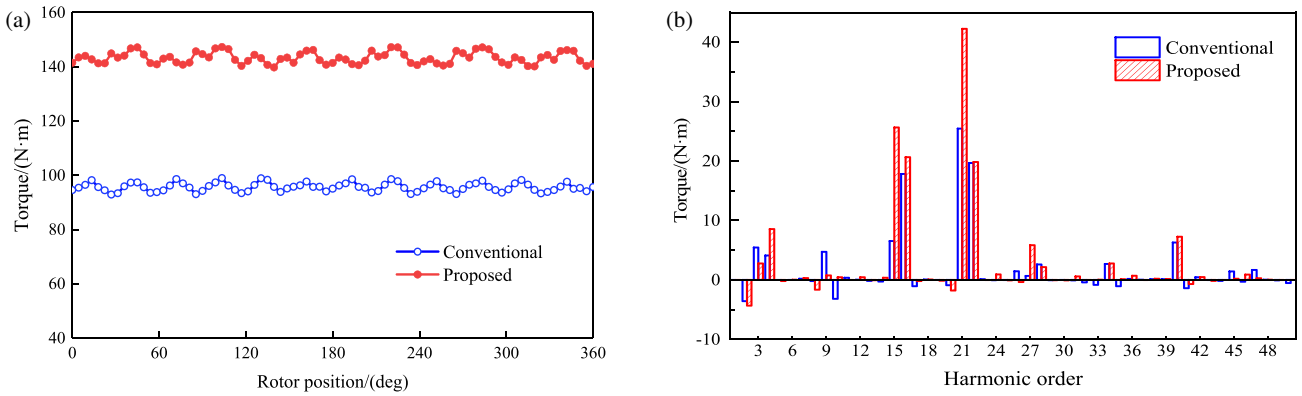

FIGURE 13. Output torque.

TABLE 4. The values of power factor.

	Unit	Conventional	Proposed
Phase flux linkage	Wb	0.14	0.19
Synchronous inductance	mH	6.18	6.04
Power factor	/	0.86	0.88

where ω_e denotes the electrical angular velocity, L_s the synchronous inductance, I_s the stator current, and E_{ph} the amplitude of the back-EMF.

A comparison of the power factors is presented in Table 4. Regarding synchronous inductance, the proposed machine in this paper demonstrates a value of 6.04 mH, which is closely aligned with the 6.18 mH of the conventional machine. Nevertheless, the proposed machine exhibits a higher phase flux linkage, resulting in a greater fundamental amplitude of the back-EMF than that of the conventional machine. Consequently, the power factor of the proposed machine reaches 0.88, which represents an approximate increase of 2.33% compared with the conventional machine value of 0.86.

5. CONCLUSION

In this paper, a novel MT-FSPM machine is proposed and analyzed. The main contributions are as follows:

1) Radially magnetized PMs are placed in the stator teeth in an alternating pole configuration. This study reveals that the two types of PMs respectively produce flux-reversal and flux-switching effects. The strong coupling of the synergistic effect under no-load flux linkage is verified, which effectively improves the PM utilization.

2) HTS bulk materials are arranged in the stator teeth in the same alternating pattern as the PMs. Leveraging the magnetic flux shielding effect, the HTS bulks effectively reduce tooth flux leakage, thereby enhancing the air-gap flux density amplitude and increasing torque.

3) Based on the multi-objective optimization results, the proposed machine enhances the amplitude of the primary working harmonics, achieving a 49.69% increase in output torque compared with the conventional machine. In addition, the proposed machine demonstrates superior overload capacity and power factor.

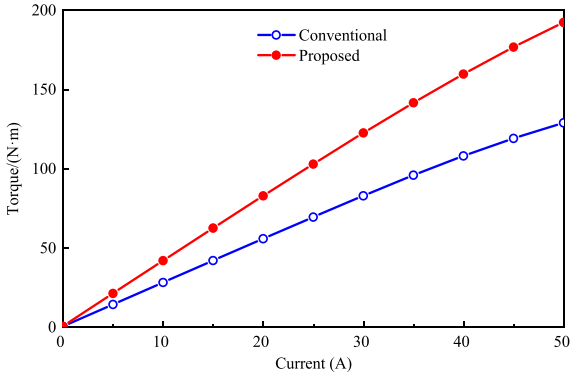

FIGURE 14. Overload capability.

It should be noted that the 2D FEA adopted in this study represents a necessary simplification to enable efficient multi-objective optimization, given the high computational cost of three-dimensional (3D) FEA, especially when coupled with genetic algorithms. Nevertheless, the end leakage flux and the 3D distribution of the HTS bulks may have non-negligible influences on the actual electromagnetic performance. Therefore, a 3D FEA will be conducted in the next step to quantify the end effects.

ACKNOWLEDGEMENT

This work was supported by the National Natural Science Foundation of China (52477056).

REFERENCES

[1] Zhang, X., T. Li, X. Wang, D. Zhou, and Z. Deng, "The magnetic levitation properties of YBCO bulks induced by a recycling SmBCO seed crystal," *IEEE Transactions on Applied Superconductivity*, Vol. 34, No. 8, 1–4, Nov. 2024.

[2] Lu, M. and R. Cao, "Comparative investigation of high temperature superconducting linear flux-switching motor and high temperature superconducting linear switched reluctance motor for urban railway transit," *IEEE Transactions on Applied Superconductivity*, Vol. 31, No. 5, 1–5, Aug. 2021.

[3] Manolopoulos, C. D., M. F. Iacchetti, A. C. Smith, K. Berger, M. Husband, and P. Miller, "Stator design and performance of superconducting motors for aerospace electric propulsion sys-

tems," *IEEE Transactions on Applied Superconductivity*, Vol. 28, No. 4, 1–5, Jun. 2018.

[4] Dong, Y., X. Li, and X. Feng, "Investigation of a novel radial partitioned stator HTS-excitation flux-switching machine," *IEEE Transactions on Applied Superconductivity*, Vol. 31, No. 5, 1–5, Aug. 2021.

[5] Saeidabadi, S., L. Parsa, K. Corzine, C. Kovacs, and T. J. Haugan, "A double rotor flux switching machine with HTS field coils for all electric aircraft applications," *IEEE Transactions on Applied Superconductivity*, Vol. 33, No. 5, 1–7, Aug. 2023.

[6] Arish, N., "Leakage flux reduction of axial-flux switching PM machine by using HTS-disk," *Physica C: Superconductivity and its Applications*, Vol. 590, 1353962, Nov. 2021.

[7] Ma, Q., A. El-Refaie, and B. Lequesne, "Low-cost interior permanent magnet machine with multiple magnet types," *IEEE Transactions on Industry Applications*, Vol. 56, No. 2, 1452–1463, Mar.-Apr. 2020.

[8] Gao, Y., M. Doppelbauer, J. Ou, and R. Qu, "Design of a double-side flux modulation permanent magnet machine for servo application," *IEEE Journal of Emerging and Selected Topics in Power Electronics*, Vol. 10, No. 2, 1671–1682, Apr. 2022.

[9] Shen, Y., Z. Zeng, Q. Lu, and Y. Li, "Investigation of a modular linear doubly salient machine with dual-PM in primary yoke and slot openings," *IEEE Transactions on Magnetics*, Vol. 55, No. 6, 1–6, Jun. 2019.

[10] Xiang, Z., S. Gui, X. Zhu, J. Wei, L. Quan, and K. Chen, "Design and analysis of a high torque performance dual-side PM vernier motor with synergetic modulation enhancement," *IEEE Transactions on Magnetics*, Vol. 60, No. 10, 1–7, Oct. 2024.

[11] Cai, S., H. Chen, X. Yuan, Y.-C. Wang, J.-X. Shen, and C. H. T. Lee, "Analysis of synergistic stator permanent magnet machine with the synergies of flux-switching and flux-reversal effects," *IEEE Transactions on Industrial Electronics*, Vol. 69, No. 12, 12 237–12 248, Dec. 2022.

[12] Chen, C., X. Ren, D. Li, R. Qu, K. Liu, and T. Zou, "Torque performance enhancement of flux-switching permanent magnet machines with dual sets of magnet arrangements," *IEEE Transactions on Transportation Electrification*, Vol. 7, No. 4, 2623–2634, Dec. 2021.

[13] Gao, Y., R. Qu, D. Li, J. Li, and G. Zhou, "Consequent-pole flux-reversal permanent-magnet machine for electric vehicle propulsion," *IEEE Transactions on Applied Superconductivity*, Vol. 26, No. 4, 1–5, Jun. 2016.

[14] Zheng, Y., L. Wu, Y. Fang, T. Li, and W. Zheng, "Comparative analysis of doubly fed flux-reversal permanent magnet machines with different PM arrangements and consequent-pole topologies," *IEEE Transactions on Magnetics*, Vol. 57, No. 2, 1–6, Feb. 2021.

[15] Wei, F., Z. Q. Zhu, H. Qu, L. Yan, and J. Qi, "New dual-PM spoke-type flux-reversal machines for direct-drive applications," *IEEE Transactions on Industry Applications*, Vol. 58, No. 5, 6190–6202, Sep.-Oct. 2022.

[16] Zhang, Z., W. Hua, Y. Wang, X. Li, X. Zhu, and M. Cheng, "Relationship between slot-pole combination and performance of partitioned-stator field-excitation brushless machines by air-gap field modulation principle," *IEEE Transactions on Transportation Electrification*, Vol. 10, No. 4, 10 410–10 419, Dec. 2024.

[17] Jing, L., T. Wang, W. Tang, W. Liu, and R. Qu, "Characteristic analysis of the magnetic variable speed diesel-electric hybrid motor with auxiliary teeth for ship propulsion," *IEEE/ASME Transactions on Mechatronics*, Vol. 29, No. 1, 668–678, Feb. 2024.